Multivariate Analysis Identifying [Cu(N∧N)(P∧P)]+ Design and Device Architecture Enables First-Class Blue and White Light-Emitting Electrochemical Cells

Luca M. Cavinato, Sarah Wölfl, Alexander Pöthig, Elisa Fresta, Claudio Garino, Julio Fernandez-Cestau,* Claudia Barolo,* and Rubén D. Costa*

White light-emitting electrochemical cells (LECs) comprising only [Cu(N∧N)(P∧P)]+ have not been reported yet, as all the attempts toward blue-emitting complexes failed. Multivariate analysis, based on prior-art [Cu(N∧N)(P∧P)]+-based thin-film lighting (>90 papers) and refined with computational calculations, identifies the best blue-emitting [Cu(N∧N)(P∧P)]+ design for LECs, that is, N∧N: 2-(4-(tert-butyl)phenyl)-6-(3,5-dimethyl-1H-pyrazol-1-yl)pyridine and P∧P: 4,5-bis(diphenylphosphino)-9,9-dimethylxanthene, to achieve predicted thin-film emission at 490 nm and device performance of 3.8 cd A^{-1}@170 cd m^{-2}. Validation comes from synthesis, X-ray structure, thin-film spectroscopic/microscopy/electrochemical characterization, and device optimization, realizing the first [Cu(N∧N)(P∧P)]+-based blue-LEC with 3.6 cd A^{-1}@180 cd m^{-2}. This represents a record performance compared to the state-of-the-art tricoordinate Cu(I)-complexes blue-LECs (0.17 cd A^{-1}@20 cd m^{-2}). Versatility is confirmed with the synthesis of the analogous complex with 2-(4-(tert-butyl)phenyl)-6-(3,5-dimethyl-1H-pyrazol-1-yl)pyrazine (N∧N), showing a close prediction/experiment match: λ = 590/580 nm; efficiency = 0.55/0.60 cd A^{-1}@30 cd m^{-2}. Finally, experimental design is applied to fabricate the best white multicomponent host:guest LEC, reducing the number of trial-error attempts toward the first white all-[Cu(N∧N)(P∧P)]+-LECs with 0.6 cd A^{-1}@30 cd m^{-2}. This corresponds to approximately ten-fold enhancement compared to previous LECs (<0.05 cd A^{-1}@<12 cd m^{-2}). Hence, this work sets in the first multivariate approach to design emitters/active layers, accomplishing first-class [Cu(N∧N)(P∧P)]+-based blue/white LECs that were previously elusive.

1. Introduction

Light-emitting electrochemical cells (LECs) are the simplest thin-film lighting source featuring single and ion-based active layer prepared via low-cost solution-based technologies using air-stable electrodes.[1,2] Upon biasing, LECs exhibit efficient ion-assisted charge injection by forming electric double layers (EDLs) at the electrode interfaces and ion-controlled growing of the p-/n-doped fronts, while the electron–hole recombination occurs at the intrinsic neutral zone (i) of a dynamically formed p–i–n junction.[3] The versatility of LECs lies on the myriad of suitable emitters (conjugated polymers (CPS),[4] ionic transition metal complexes (iTMCs),[5] small molecules (SMs),[6] Cd-based quantum dots (QDs),[7] etc.)[8,9] and electrolytes (ionic liquids (ILs), inorganic salts, etc.),[10] as well as the possibility of fabricating devices with arbitrary 3D shapes. LECs are, therefore, regarded as monochromatic sources appealing for labeling, sensing, and smart lighting applications.[2,11,12]

Notwithstanding, the lack of bright and stable emitters for blue-LECs strongly hinders high performing white devices,

L. M. Cavinato, S. Wölfl, E. Fresta, J. Fernandez-Cestau, R. D. Costa
Chair of Biogenic Functional Materials
Technical University of Munich
Schulgasse 22, 94315 Straubing, Germany
E-mail: julio.fernandez-cestau@tum.de; ruben.costa@tum.de

The ORCID identification number(s) for the author(s) of this article can be found under https://doi.org/10.1002/adma.202109228.

A. Pöthig
Department of Chemistry & Catalysis Research Center (CRC)
Technical University of Munich
Lichtenbergstr. 4, 85747 Garching, Germany

C. Garino, C. Barolo
Department of Chemistry
University of Turin
Via Giuria 7, Turin 10125, Italy
E-mail: claudia.barolo@unito.it

C. Garino, C. Barolo
NIS Interdepartmental Centre and INSTM Reference Centre
University of Turin
Via Gioacchino Quarello 15/a, Turin 10125, Italy

C. Barolo
ICxT Interdepartmental Centre
University of Turin
Lungo Dora Siena 100, Turin 10153, Italy

representing a major milestone in the field.[13,14] Here, LECs with blue-emitting Ir-iTMCs are moderate performing due to the significant degradation via population of metal centered excited states: average stabilities of <90 min at efficiencies <2.2 cd A^{-1}@115 cd m^{-2}.[5] The high cost and low abundance of iridium in the Earth's crust mandate research of higher performing and more sustainable high-energy emitters. Despite efforts, none of the abovementioned emitters have led to blue-LECs outperforming those with Ir-iTMCs: average stabilities of <5 min at 0.4 cd A^{-1}@10 cd m^{-2}, <1 h at 0.5 cd A^{-1}@10^2 cd m^{-2}, ≈10 s at 4.5 cd A^{-1}@10^3 cd m^{-2}, for QD-, SM-, and CP-LECs, respectively.[13]

As far as high-energy emissive iTMCs are concerned, Cu-iTMCs have been explored as a promising alternative to Ir-iTMCs over the last decades.[15,16] Blue Cu-iTMC-LECs have been only achieved with NHC-based Cu-iTMCs (NHC is N-heterocyclic carbene ligand in combination with N^N ligands in tricoordinate complexes; [Cu(NHC)(N^N)]$^+$), showing stabilities of <5 min at 0.17 cd A^{-1}@20 cd m^{-2}.[17,18] Surprisingly, though different groups have designed blue-emitting [Cu(N^N)(P^P)]$^+$ bearing wide band gap N^N ligands, none of them led to functional blue LECs and organic light-emitting diodes (OLEDs) without involving a host:guest approach.[19–24] In contrast, solid empirical relationships between the X-ray structures (i.e., weak intra- and inter-molecular interactions between ligands in the complexes [O···H between P^P and N^N ligands, CH–π, π–π, etc.], buried volumes, ligand distortions [dihedral angles, bite angles/distances to metal ion, etc.] and the photoluminescence features (i.e., maximum emission wavelength (λ_{max}), photoluminescence quantum yields (PLQY), etc.) in crystalline powder have been established.[15,16,25–29] However, these rules do not apply to rationalize the photoluminescence of their respective thin-films prepared via solvent-based deposition techniques as well as to predict device performance (color, efficiency, luminance, etc.). This is related to unforeseen changes of the structure of Cu-iTMCs induced by environment surrounding the in thin films, while structural analysis of these thin-films is very tedious.[30–32] Indeed, it is common that the PLQY is strongly reduced and the emission color changes compared to those in the crystalline form. Hence, we are lacking a fundamental rationale for direct correlation between the molecular/electronic structures of [Cu(N^N)(P^P)]$^+$ and their final photo-/electroluminescent figures-of-merit in thin-films/devices to realize all-Cu-iTMCs white LECs, in general, and [Cu(N^N)(P^P)]$^+$-based blue LECs, in particular.

In this context, the innovative aspect of this work is the successful implementation of the multivariate analysis method to decipher the first [Cu(N^N)(P^P)]$^+$ design for blue LECs with an outstanding performance compared to other blue devices regardless of the abovementioned emitters. Our dataset consisted in all the [Cu(N^N)(P^P)]$^+$ complexes applied to thin-film lighting devices up to date (>90 contributions).[15,16] We recognized an incredibly high correlation between the X-ray structural and electronic parameters of [Cu(N^N)(P^P)]$^+$ with their photoluminescence in thin-films (λ_{max} and PLQY) and the device performance (efficiency and luminance). The multivariate approach indicated that the most promising high-energy emitting complexes belong to those bearing the pyridine-pyrazole N^N ligand. The substituents of this ligand were further refined analyzing the calculated structural/electronic features to predict the above figures-of-merit. Among the investigated structures, the [Cu(N^N)(P^P)]$^+$ design that maximized both photoluminescence in thin-film and device performance was: [Cu(Xanthphos)(N^N^{py})][PF$_6$] (1)—**Figure 1**; Xanthphos is 4,5-bis(diphenylphosphino)-9,9-dimethylxanthene, N^N^{py} is 2-(4-(tert-butyl)phenyl)-6-(3,5-dimethyl-1H-pyrazol-1-yl)pyridine. The synthesis, X-ray structural analysis, photoluminescence/electrochemistry/microscopy studies in thin-films, and the device optimization nicely confirmed the success of the multivariate analysis. In particular, 1 is the first high-energy emissive [Cu(N^N)(P^P)]$^+$ (λ_{max} = 470 nm; PLQY of 42%) that leads to blue LECs featuring remarkable performance (3.6 cd A^{-1}@180 cd m^{-2}) as predicted by the model (λ_{max} = 488 nm; PLQY of 47%; device efficiency 3.8 cd A^{-1}@170 cd m^{-2}).

The perfect correlation between the multivariate analysis and the photo-/electroluminescence behavior of Cu-iTMC thin-films was further validated with the design of a close related analogue, namely [Cu(Xanthphos)(N^N^{pz})](PF$_6$) (2)—Figure 1; N^N^{pz} is 2-(4-(tert-butyl)phenyl)-6-(3,5-dimethyl-1H-pyrazol-1-yl)pyrazine. The model predicted thin-film emission centered at 583 nm associated to PLQYs of 25% and devices showing 0.55 cd A^{-1}@30 cd m^{-2}, while the experimental values were 575 nm, 20%, and 0.6 cd A^{-1}@30 cd m^{-2}. This nicely confirms the potential of this approach to design Cu-iTMCs for thin-film lighting applications, such as LECs without the need of numerous trial-error attempts or tedious complex structural analysis of the Cu-iTMCs films.

Beyond the abovementioned achievements, an experimental design based on an analogous multivariate approach
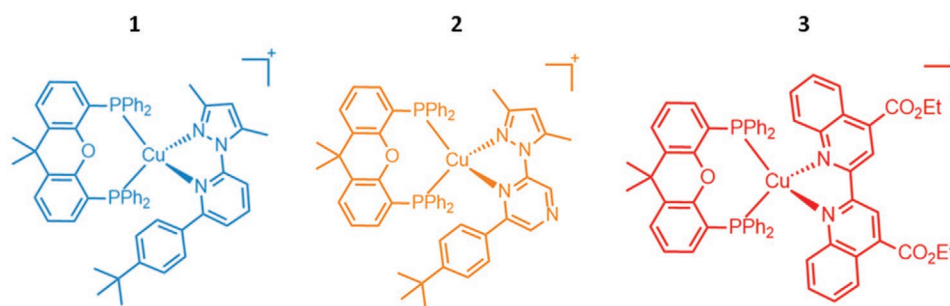

Figure 1. Chemical structures of complexes 1–3.

**ADVANCED
SCIENCE NEWS**

www.advancedsciencenews.com

**ADVANCED
MATERIALS**

www.advmat.de

was also applied to identify the optimal active layer composition in a tricomponent host:guest approach to realize the first all-Cu-iTMCs white LECs using **1**, **2**, and the red-emitting [Cu(Xanthphos)(dcbq)](PF$_6$) complex (**3**)—Figure 1; dcbq is 4,4′-diethylester-2,2′-biquinoline.[33] The optimized LEC showed a white emission corresponding to x/y CIE color coordinates of 0.30/0.35 and color rendering index (CRI) of 90 as well as efficacies of 0.6 cd A^{-1}@30 cd m^{-2}. This represents an almost ten-fold enhancement compared to the previous state-of-the-art of white-emitting Cu-iTMC:SM-based LECs: 0.05 cd A^{-1}@12 cd m^{-2} with x/y CIE color coordinates of 0.30/0.30 and CRI of 90.[34] In addition, taking into account white host:guest LECs with CRI values >90 as white color quality, the first all-Cu-iTMCs white LECs stand out those with CPs, QDs, SMs, and Ir-iTMCs with (i.e., averages <0.3 cd A^{-1}@<70 cd m^{-2}).[13,35] Hence, this work sets in the successful use of multivariate analysis as a relatively easy tool for designing emitters and active layers for first class blue/white [Cu(N^N)(P^P)]$^+$-based LECs.

2. Results and Discussion

A large dataset collecting 15 inputs related to the most relevant X-ray structural features (buried volumes, bite angles, metal–ligand bond lengths, Cu–O distances, and ligand torsion angles) and electronic aspects (HOMO–LUMO levels, ligand polarizability and hydrophobicity) of over 90 [Cu(N^N)(P^P)]$^+$ employed in both, LECs and OLEDs, was built.[15,16] As the model responses, the photoluminescence features in thin-films (λ_{max} and PLQYs) and electroluminescence features (maximum efficacies and luminances) were taken into account as their maximum values are 1) commonly reported, 2) heavily dependent on the device configuration and driving conditions, and 3) not correlated in time—see Experimental Section for further details. The partial least squares regression (PLS) analysis led to a nearly impressive statistical correlation ($R^2 > 0.92$), suggesting that simple linear combinations based on first and second order terms taking into account both the X-ray structures and electronic parameters are good enough to predict the abovementioned thin-film photo-/electroluminescent outputs covering the whole visible range—**Figure 2**. Indeed, the normalized residual standard deviations of different responses are always <3, inferring the absence of outliers—Figure S1, Supporting Information.

This method drives the designing rules for [Cu(N^N)(P^P)]$^+$ complexes applied to thin-film lighting, allowing us to analyze the normalized effects of the abovementioned structural/electronic factors as well as their interactions on the desired outputs—Figure S2, Supporting Information. Based on the analysis, we can state that a proper complex design toward highly
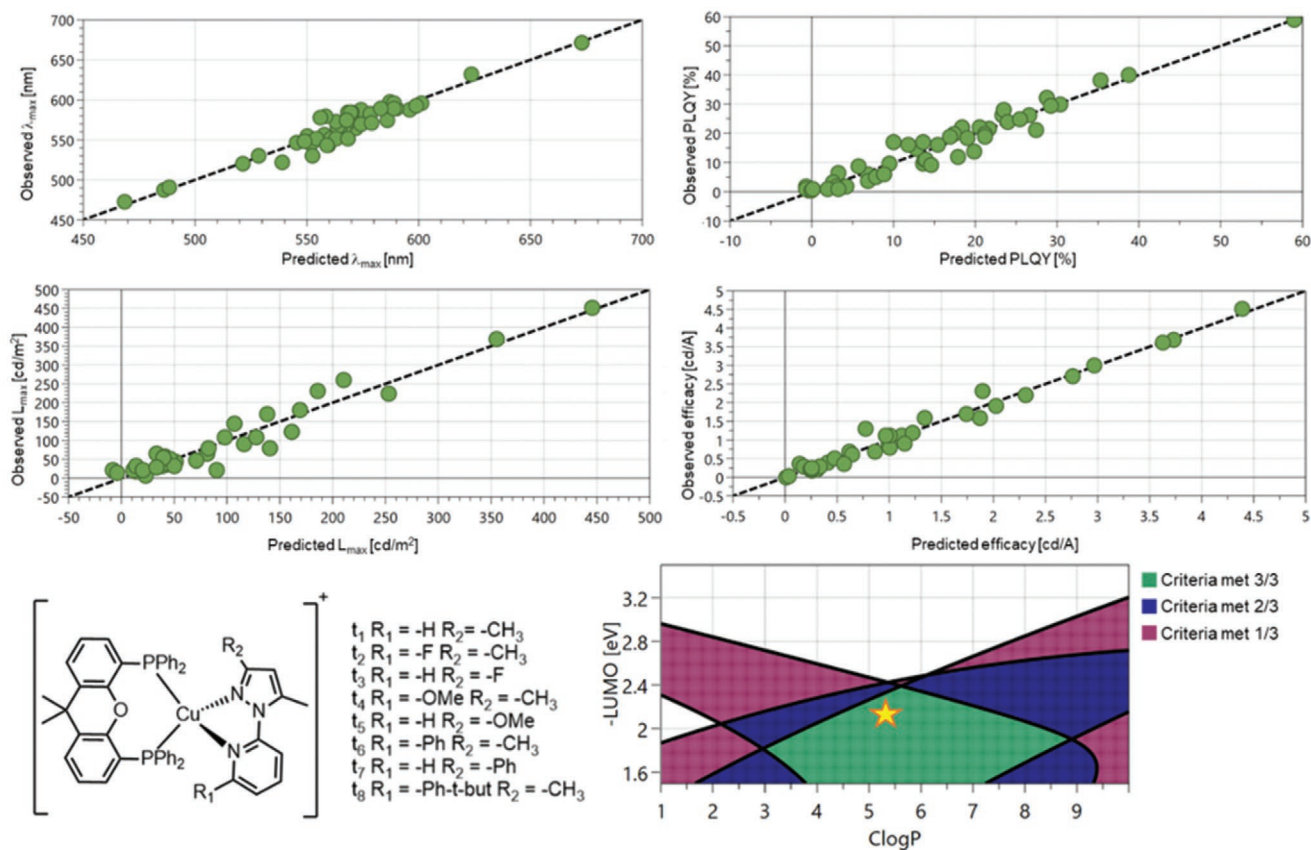

Figure 2. Top: observed versus predicted responses of the multivariate method, showing relative R^2 of 0.92, 0.95, 0.93, and 0.98 for λ_{max} (top-left), PLQY (top-right), luminance (center-left), and efficiency (center-right), respectively. Bottom: Chemical structures of the eight complexes simulated to refine the N^N ligand with respect to peripheral substituents (left) and the position of complex t$_8$ or **1** (yellow star) in the experimental space with respect to selected criteria: λ_{max} < 500 nm, PLQY of 0.3–1, efficiency > 2 cd A^{-1}.

emissive thin-films and performing devices should not be limited to first-order linear correlations as they are less significant than second-order ones—vide infra. Moreover, traditional trial-error approaches focused on the deep study of only one variable per time toward rationalizing and optimizing Cu-iTMCs for thin-film lighting might easily fail,[15,16] forgetting the significance of the second-order interaction terms. Based on the results of this multivariate analysis, it is now much simpler to understand the most important parameters and their intercorrelations that affect the above desired outputs as described as follows. Regarding the λ_{max} of emission of the thin films, the meaningful terms are only second order interactions between: 1) Cu···O distance and Cu···P^P ligand distance/bite angle P^P ligand, 2) torsion angle of N^N ligand and HOMO level, and 3) the LUMO level and the total/P^P ligand buried volumes. Specifically longer Cu···O distances associated with either longer Cu···P^P ligand distances or wider bite angles of the P^P ligand as well as deeper HOMO levels associated with high torsion N^N angles will lead to strongly red-shifted emissions. By contrast, at defined LUMO level, increasing the total and the P^P ligand buried volumes will shift the emission toward higher energy regions. In contrast, the enhancement of the PLQY goes hand-in-hand with the increase of the total buried volume and the Cu···O distance (first order positive relationship), nevertheless they are not synergistic—Figure S2, Supporting Information. In other words, the strategy for improved PLQY in Cu-iTMCs enhancing both parameters at the same time is unsuccessful due to a minimal positive contribution of the interaction between the two variables. However, there are other significant second order interactions. On one hand, increasing the buried volume of the P^P ligand while stabilizing the energy of the HOMO and LUMO levels will strongly reduce the PLQY. At a fixed HOMO level, it is advisable to use P^P ligands with small buried volume if high-energy emissive [Cu(N^N)(P^P)]+ complexes (higher LUMO level) are desired. On the other hand, longer Cu···O distances associated with longer Cu···P^P ligand distances or deeper HOMO levels negatively affect the PLQY. In addition, longer Cu···P^P ligand distances coupled with wider bite angles of N^N ligand are beneficial for the PLQY. Thus, it is more accurate to state that for defined P^P and N^N ligands there is an optimal Cu···O distance that maximizes the PLQY response for each emitting region.

As far as the device performance is concerned, both maximum luminance and efficiency levels are linked meaningfully to second-order interactions between 1) Cu···O distances and HOMO/LUMO levels and 2) bite angle of N^N ligands and HOMO levels—Figure S2, Supporting Information. For instance, the interaction between the latter shows a positive linear correlation for luminance and efficiency. Hence, deeper HOMO levels could enhance device performances if associated with wider bite angles of N^N ligands. However, a more stable HOMO associated with a longer Cu···O distance is detrimental, in line with the negative correlation toward enhanced PLQYs—vide supra. All of the aforementioned represents the most important findings noted in our analysis. However, we are currently working on several models/approaches to get a deeper understanding.

Despite the complexity of this analysis, the few examples meeting structural and electronic features that maximize all the above outputs in the high-energy part of the spectrum are complexes based on Xantphos as P^P and pyridine-pyrazole for the N^N family. Thus, we decided to fine-tune the N^N core with standard substituents of different nature (alkyl, phenyl, halogen, etc.) located at 2 and 8 positions (test complexes t_{1-8} shown in Figure 2). Density functional theory (DFT) was applied to calculate their electronic and structure features in the ground state—see Experimental Section. The multivariate model was applied to them to predict λ_{max}, PLQY, luminance, and efficiency. As a result, complex t_8 (hereafter named **1** as shown in Figure 1) with 4,5-bis(diphenylphosphino)-9,9-dimethylxanthene and 2-(4-(tert-butyl)phenyl)-6-(3,5-dimethyl-1H-pyrazol-1-yl)pyridine as P^P and N^N^{py} ligands was the only candidate sitting on the so-called sweet spot, in which the criteria λ_{max} < 500 nm, PLQY of 0.3–1, efficiency > 2 cd A^{-1} are simultaneously met—Figure 2. The positions of the other complexes t_{1-7} in the experimental space with respect of the defined criteria are provided in Figure S3, Supporting Information. Finally, as cross-check reference, we studied the close analogue complex **2** with 2-(4-(tert-butyl)phenyl)-6-(3,5-dimethyl-1H-pyrazol-1-yl)pyrazine as N^N^{pz} ligand to validate the experimental/predicted match of the photo-/electroluminescent parameters using the multivariate model.

The syntheses of N^N^{py} and N^N^{pz} ligands were adapted from the procedure reported elsewhere.[36,37] The targeted copper(I) complexes were isolated as white (**1**) or yellow (**2**) microcrystalline solids in good yields (77%) following a standard 2-steps/1-pot method in dichloromethane (DCM) at room temperature—see Experimental Section for details of the synthesis and spectroscopic characterization.[38] Single crystals suitable for X-ray diffraction experiments of **1** and **2** were obtained by slow diffusion at room temperature of Et$_2$O vapor in a saturated solution of the corresponding crude in DCM. Details of the data collection, solution, and refinement of the structures are collected in the Experimental Section, while the CIF files are deposited in the CCDC database.

Ellipsoid representations are presented in Figure S4, Supporting Information, and the most relevant bond lengths, angles, and crystallographic data are listed in Tables S1–S3, Supporting Information. Both complexes showed four-coordinate geometry index (τ_4) of 0.76 corresponding to a hybrid geometry between trigonal pyramidal (C$_{3v}$, τ_4 = 0.85) and seesaw (C$_{2v}$, τ_4 = 0.64).[39] The P^P bite angles are in the typical range of Xanthphos-derived Cu-iTMCs, while the bite angles of the N^N ligand are shorter (75.84° and 73.97° for **1** and **2**, respectively) compared to standard bipyridine systems (≈80°).[9,15] This is attributed to the high value of torsion angle between the pyridine and pyrazole moieties—22.62° (**1**) and 25.94° (**2**). In **2**, the presence of an electron-withdrawing atom in *para*-position weakens the bond between the metal ion and the pyridine ring, enhancing the intra ring distortion of the N^N ligand. The Cu−N bond lengths are longer in **2** compared to **1** (2.3516 vs 2.2558 Å), while the Cu−O bond lengths are shorter (2.939 vs 3.045 Å). Finally, the X-ray structures and those calculated by DFT are in good agreement—Table S3, Supporting Information. Likewise, the electronic features calculated for **1** and **2** (HOMO/LUMO levels of 6.0 eV/−2.0 eV and −6.0 eV/−2.7 eV, respectively) are also in line with those measured by cyclic voltammetry—see Experimental Section. In short, Figure S5,

**ADVANCED
SCIENCE NEWS**

www.advancedsciencenews.com

**ADVANCED
MATERIALS**

www.advmat.de

Supporting Information, displays quasi-reversible Cu(I)/Cu(II) oxidation and N^N ligand reduction waves at 0.90 V/–2.52 V (**1**) and 0.93 V/–1.64 V (**2**) versus Fc/Fc$^+$ that are related to HOMO/LUMO energies of –5.7 eV/–2.2 eV (**1**) and –5.7 eV/–3.1 eV (**2**) with respect to vacuum. As expected, the presence of the N-substitution in *para*-position lowers the LUMO without affecting the HOMO, leading to a reduced band gap in **2**.

Since experimental and DFT structural/electronical parameters match, similar experimental/predicted photo-/electroluminescence parameters are anticipated if the multivariate analysis tool is effective. The predicted thin-film photoluminescence values (λ_{max}/PLQY) are 488 nm/47% and 583 nm/25% for **1** and **2**, respectively. In view of the fact that the literature used in the dataset is mostly related to the photo-/electroluminescence data of thin-films with the standard IL 1-butyl-3-methyl-imidazolium hexafluorophosphate (BMIMPF$_6$; molar ratio 1:4 with respect to complex), we prepared sets with **1** and **2** as pristine and **1/2**:IL as doped thin-films ($\approx$120 nm) using spin-coating technique—see Experimental Section.

Atomic force microscopy (AFM) images showed a neat and homogeneous morphology with root mean square (RMS) roughness values of $\approx$150 pm over an area of 100 μm^2 for pristine **1** and blend **1**:IL films—Figure S6, Supporting Information. By contrast, those with **2** display a homogenous layer with some aggregation features, leading to RMS roughness of $\approx$2150 pm and $\approx$950 pm for **2**-pristine and **2**:IL thin-films, respectively. Nevertheless, those films are suitable for photoluminescence studies and device implementation.

1- and **2**-pristine films featured blue and yellow emission bands centered at 490 and 590 nm and associated to PLQYs of 40% and 25% and long excited state lifetime values (τ) of 262 and 15 μs, respectively. Importantly, films with IL feature slightly blue-shifted emission (470 nm/575 nm) retaining PLQYs (42%/20%) for **1** and **2**, respectively—Table S4, Supporting Information. Thus, the k_{rad} and k_{nrad} in **1**-based films at room temperature are of the same order of magnitude while, **2**-based films showed larger k_{nrad} (Table S4, Supporting Information). The perfect match between the predicted and experimental values confirms that the multivariate method is successful in correlating the X-ray structural parameters and electronic features with the photoluminescence of their thin films.

To gain insight into the photoluminescence mechanism, the geometries of the first singlet and triplet excited states (S$_1$ and T$_1$) were fully relaxed at the DFT level. In both complexes, the nature of first excited states is correlated to HOMO $\rightarrow$ LUMO electronic transition with a strong charge transfer character (Figure S7, Supporting Information). According to the relative energy level, the substitution of pyridine ring (**1**) with a pyrazine one (**2**) leads to a great stabilization of the S$_1$ and T$_1$ states of $\approx$0.5 eV. In addition, the S$_1$–T$_1$ energy splitting ($\Delta E_{S1–T1}$) of both complexes is small enough (<0.15 eV) to allow a TADF emission mechanism, while phosphorescence could also be present.[15] This was further studied with temperature dependent photoluminescence of neat and IL-doped **1**- and **2**-films. In general, the temperature increase from 77 to 420 K leads to a hypsochromic shift of the $E_{0–0}$ band ($\approx$19 nm) for **1**-/**2**-pristine films, implying that the emission may arise from two excited states in thermal equilibrium. Importantly, the τ of **1** drastically changes spanning from 1.5 ms at 77 K to 262 μs at

room temperature—**Figure 3** and Figure S8 and Table S4, Supporting Information. In the other systems, the τ exhibited one-fold shorter changes compare to pristine **1** films. For instance, **1**:IL films show τ of 840 μs at 77 K and 245 μs at room temperature and **2**-pristine/**2**:IL film display τ of 206/347 μs at 77 K and 15/32 μs at room temperature.

In all cases, the temperature dependence of τ follows a Boltzmann-type equation, Equation (1):

$$\tau = \frac{3 + e^{\left(\frac{-\Delta E(S_1 - T_1)}{k_b T}\right)}}{3k(T_1) + k(S_1) \times e^{\left(\frac{-\Delta E(S_1 - T_1)}{k_b T}\right)}} \tag{1}$$

where k_b is the Boltzmann constant, $\Delta E(S_1–T_1)$ the energy separation between the two states, and $k(S_1)/k(T_1)$ the radiative constant of prompt fluorescence/phosphorescence, respectively.

A good fit (R^2 > 0.98) in the 77–420 K temperature range was obtained. The extrapolated values are $\tau(S_1)$ = 3.6 μs/243 ns and 202 ns/14 ns, $\tau(T_1)$ = 1.4 ms/828 μs and 206 μs/344 ns, and $\Delta E(S_1–T_1)$ = 0.09/0.16 eV and 0.08/0.16 eV for neat/IL-doped **1** and **2** films, respectively. Further confirmation of the good-quality fit is the extrapolated $\tau(T_1)$ values that are close to those noted at 77 K, where the phosphorescence process is dominant. To fully visualize the individual contributions of phosphorescence and TADF emission contributions relative to the total emission intensity (I_{tot}), we applied Equation (2):

$$\frac{I(S_1)}{I(T_1)} = \frac{k(S_1)}{3 \times k(T_1)} \times e^{\left(-\frac{\Delta E(S_1 - T_1)}{K_b T}\right)} \tag{2}$$

where $I(S_1)$ is the TADF intensity originated from the singlet state S$_1$ and $I(T_1)$ the phosphorescence intensity from the triplet state T$_1$. Figure S9, Supporting Information, shows that TADF comprises the 83% and 92% of the total emission for neat **1**- and **2**-films, respectively. Even if the TADF process is slightly favorable in **2** compared to **1** in thin-film, the former shows a prominent thermal quenching, suggesting an efficient concomitant thermal activation of nonradiative processes as expected from the low PLQY and τ values—Figure S10, Supporting Information. Thus, less efficient devices are expected with **2**. The higher $\Delta E_{S1–T1}$ and the lower TADF contribution for **1** with respect of **2** are in line with its longer excited state lifetime at room temperature.

Finally, it is interesting to pinpoint how the use of IL additives also reduces the TADF contribution to 66%/90% for IL-doped **1/2** films at room temperature. This has not been discussed in the literature and could be attributed to molecular distortions promoted by short-range interactions between the IL and the complexes at the edges of the microcrystalline domains of the thin films.[32] This rationale must be, however, considered as qualitative and more experimental findings are needed to get a deeper understanding.

Next, LECs were fabricated with a double-layered architecture ITO/PEDOT:PSS (70 nm)/active layer (120 nm)/Al (90 nm) and analyzed monitoring the luminance, color, and electrical behavior over time at pulsed current densities of 10 and 150 mA cm^{-2} (1 kHz block wave and 50% duty cycle) as this
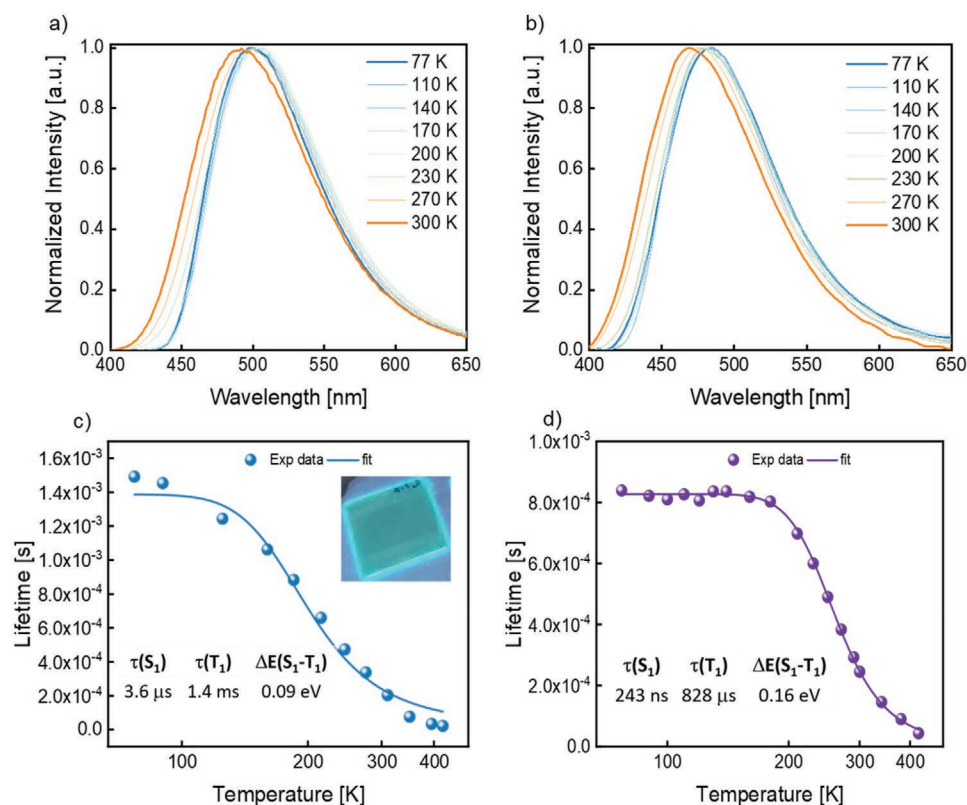
**ADVANCED
SCIENCE NEWS**

www.advancedsciencenews.com

**ADVANCED
MATERIALS**

www.advmat.de

Figure 3. Top: Emission spectra of **1**-based (a) and **1**:IL-based (b) thin-films recorded at different temperatures—see legend. Bottom: τ values of **1**-based (c) and **1**:IL-based (d) thin films versus temperature. The solid lines represent the fit curves according to Equation (1), while the extrapolated parameters are provided. Inset in (c): **1**-based thin film under UV lamp (λ_{exc} = 305 nm).

driving scheme has led to best performing LECs to date—see Experimental Section.[4,9] At low applied currents, pristine **1**-devices featured lack of charge injection over time. At pulsed 150 mA cm^{-2}, the typical LEC behavior with an instantaneous blue emission (x/y CIE color coordinates of 0.21/0.34) associated to an instantaneous luminance value of 10 cd m^{-2} that increases up to 205 cd m^{-2} and an initial average voltage (9 V) that exponentially reduces to a plateau of 7 V were noted—**Figure 4** and **Table 1**. The quick decrease of the average voltage is related to the electrochemical doping promoted by the formation of EDLs at the electrode interface, while the voltage plateau indicates the lack of a severe electrochemical degradation (over oxidation/reduction processes).[40] Indeed, the formation of dark spots was not noted as expected from the good film morphology—vide supra.[41] Importantly, the photo-/electroluminescence band shape are the same (E_{0-0} of 2.92 eV and FWHM of 90 nm), indicating that the same excited state is involved regardless of the photo/electrical excitation process over time. Unfortunately, the devices exhibited a slow color corruption toward the yellowish region (x/y CIE color coordinates of 0.28/0.41) with a broad emission band (FWHM = 145 nm; E_{0-0} = 2.90 eV) centered at 550 nm. This finding is independent of the device self-heating (42 °C at pulsed 150 mA cm^{-2}) under operation conditions—Figure S11, Supporting Information.[42] In addition, since the E_{0-0} values holds, the color shift must be related to: 1) microcavity and scattering effects,[43] and/or 2) strong electrical polarization due to unbalanced doping

and movement of the emitting p–i–n regions that are typically present using high applied currents.[44] Thus, it is not trivial to determine the dominant process. Finally, luminance raises corresponds to a maximum efficiency of 0.3 cd A^{-1} or external quantum efficiency of 0.11%, while the luminance quickly decreases, leading to stabilities of 1.5 min and 7.59 mJ. The poor stability could be related to: 1) quick and irreversible oxidation of Cu-iTMCs upon hole injection, forming Cu^{2+} species that are not emissive and act as carrier quenchers—Scheme S1, Supporting Information, and/or, 2) quick reduction of the emissive intrinsic region.[17] To rule out the first option, static electrochemical impedance spectroscopy (EIS) was applied to fresh and post-mortem **1**-devices to determine the changes of the LEC resistance upon increasing the applied voltage—see Experimental Section. The EIS data were fitted with the equivalent circuit shown in Figure S12, Supporting Information, and the extrapolated key parameters are summarized in Table S5, Supporting Information. They showed typical LEC electrical behavior with regards to both, resistance versus voltage profile and resistance value regime, indicating that the irreversible formation of oxidized species is not detrimental.

These findings suggest that stable blue LECs could be achieved using lower pulsed currents. Thus, devices with **1**:IL active layers were investigated as ILs assist in managing charge injection and doping growths at low applied currents.[4,9] As expected, these devices were functional at pulsed current densities of 10 mA cm^{-2} with an average voltage plateau at 5.5 V and
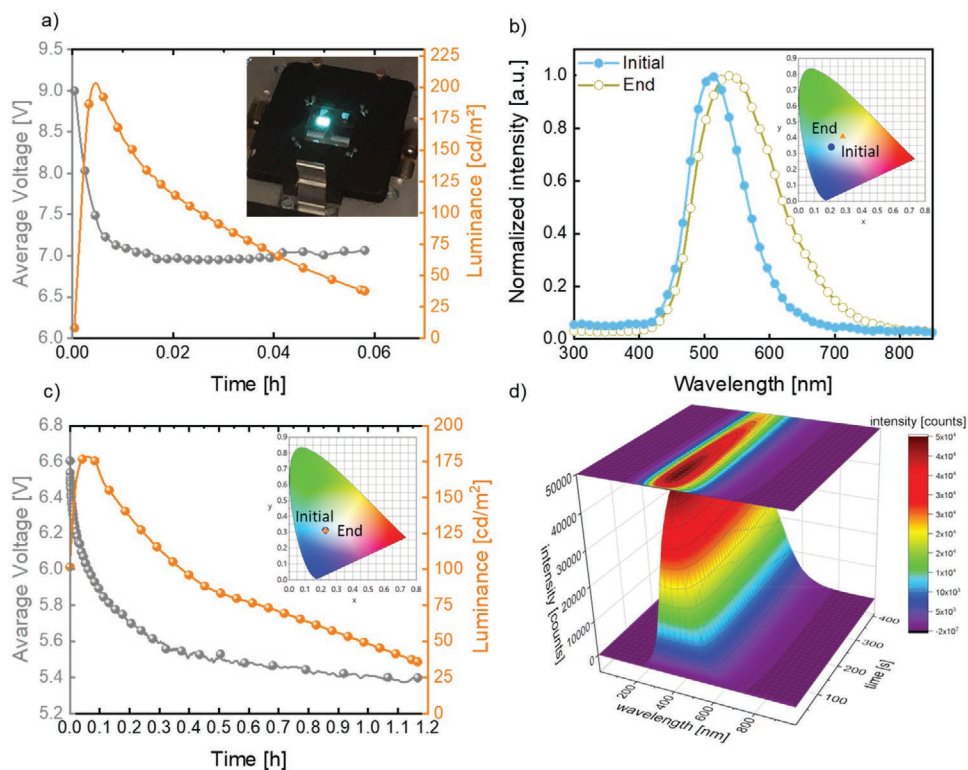
Figure 4. a,c) Luminance and average voltage for **1**-based (a) and **1**:IL-based (c) devices measured using a pulsed 150 and 10 mA cm^{-2}, respectively. b) Initial and end-life electroluminescence response of **1**-based device, and d) electroluminescence response over time of **1**:IL-based device. The insets show a picture of **1**-based device in operando (a) as well as initial and end-life x/y CIE coordinates of **1**-based (b) and **1**:IL-based (c) devices.

luminance raises from an instantaneous value of 100 cd m^{-2} up to ≈180 cd m^{-2}. This corresponds to a maximum efficiency value of 3.6 cd A^{-1} (EQE = 1.2%), that could be considered as a first-class in Cu-iTMC-LECs regardless of the color emission.[13,15,16] What is more, these values correspond to a blue emission band (E_{0-0} = 2.95 eV and FWHM = 100 nm) with x/y CIE color coordinates of 0.23/0.31 that is fully stable over the whole lifespan, corroborating the successful fabrication of the first blue-emitting [Cu(N^N)(P^P)]-LEC to date—Figure 4. Finally, the slow decrease of the luminance led to stabilities of 30 min and 150 mJ. EIS analysis—Figure S12 and Table S5, Supporting Information, showed that the use of ILs leads to devices with 1) similar resistance versus voltage profile, 2) increased dielectric constant (ε_r) from 4 (neat devices) to 6.5, and 3) reduced ionic conductivity (σ) from 50 nS m^{-1} (neat devices) to 6 nS m^{-1}. The increase in ε_r promotes the formation of EDLs at the electrode interface allowing charge injection at low applied currents, reaching high instantaneous luminances. The reduced σ helps

to hold the width of the emissive i region, leading to more efficient devices with stable chromaticity, as the microcavity effects and self-absorption phenomena are prevented.[45] As such, we can consider that the device performance of **1**-LEC is already optimized with the use of the ILs. Thus, it is not surprising that the experimental electroluminescence parameters are in nice agreement with those predicted by the multivariate model: λ_{max} = 488 nm and 3.8 cd A^{-1}@170 cd m^{-2}.

To further confirm the above statement, we double-checked the success of the multivariate model with devices prepared with **2**. In short, pristine devices were only operative at 150 mA cm^{-2} showing 1) maximum efficiency of 0.04 cd A^{-1} (EQE 0.012%) at luminance of 30 cd m^{-2}, 2) average voltage plateau of 7 V, 3) stabilities of 2.5 min/3.2 mJ, and 4) initial orange emission (λ_{max} 580 nm with x/y CIE coordinates of 0.48/0.47) that shifts toward the red region over time (x/y CIE coordinates of 0.50/0.44)—Figure S13, Supporting Information, and Table 1. Similar to **1**-devices, the EIS analysis suggests that the poor device

Table 1. Performances of ITO/PEDOT:PSS/active Layer/Al LECs at different pulsed current density driving.

Active layer	Current density [mA cm^{-2}]	Average voltage [V]	Max. luminance [cd m^{-2}]	Max. efficiency [cd A^{-1}]	EQE [%]	Lifetime [min]	Total emitted energy [mJ]
1	150	7.0	205	0.27	0.11	1.5	7.6
1:IL	10	5.5	180	3.6	1.2	25	148
2	150	7.1	30	0.04	0.012	2.5	3.2
2:IL	10	5.9	30	0.6	0.22	5.5	4.0

**ADVANCED
SCIENCE NEWS**

www.advancedsciencenews.com
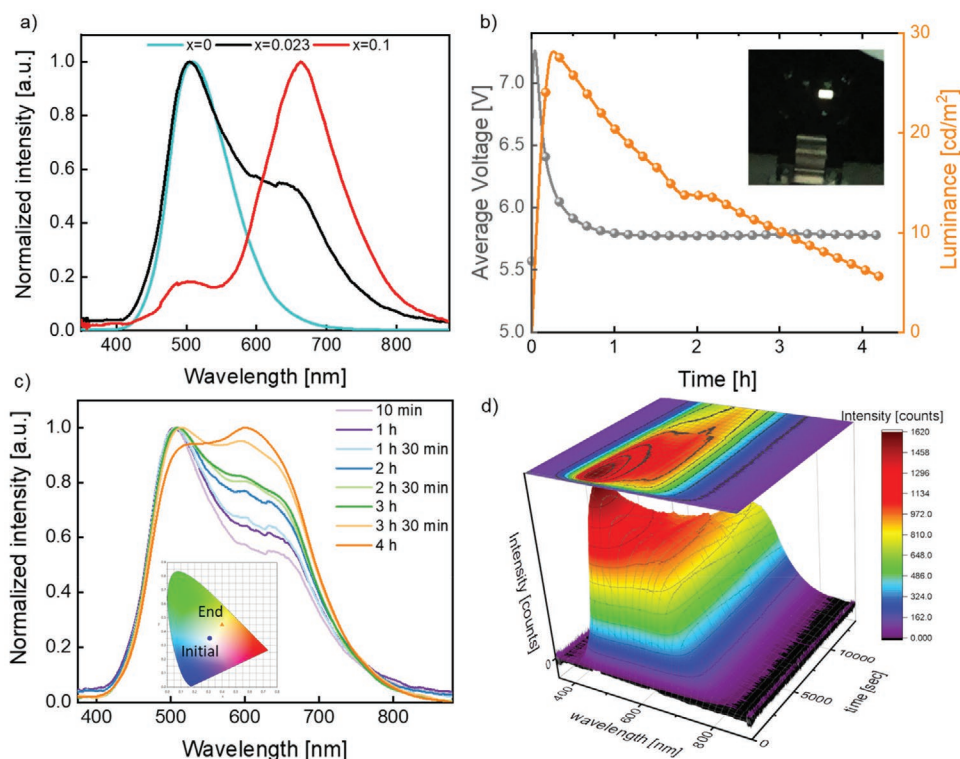
**ADVANCED
MATERIALS**

www.advmat.de

Figure 5. a) Electroluminescence spectra of LECs based on **1:3** blend with 1:0 (blue line), 0.977:0.023 (black line), and 0.9:0.1 (red line) mass ratios. Spectra are acquired at maximum luminance. b) Luminance and average voltage for LECs based on the optimum composition (**1:3** = 0.977:0.023). The inset in (b) shows the champion device in operando. c,d) Time-dependent electroluminescence spectrum of white LEC.

performance is not related to the electrochemical stability of **2**, but rather to quick collapsing of the doped regions at high applied currents—Figure S14, Supporting Information. This is confirmed by the results obtained using ILs. **2**:IL-LECs were driven at pulsed current density of 10 mA cm^{-2} showing a lack of color corruption over time (580 nm and x/y CIE color coordinates of 0.48/0.48 kept over the device lifespan) with enhanced efficiencies of 0.6 cd A^{-1} (EQE 0.22%) at luminances of 30 cd m^{-2} and stabilities of 6 min and 4.0 mJ—Figure S13, Supporting Information, and Table 1. Similar to **1**-devices, the rationale of this optimization lies on the enhanced ε_r and the reduced σ with respect to those of the pristine devices as confirmed by EIS analysis—Table S5 and Figure S14, Supporting Information. As expected, the experimental values of the optimized device are very close to those predicted by the model: 590 nm, and 0.55 cd A^{-1}@30 cd m^{-2}, confirming the success of our approach.

As a final step, we accomplished the goal to achieve the first single-layered all-Cu-iTMC white LEC. Though the emission of **1** and **2** are complementary for a host:guest strategy, a red-emitting guest (**3**; Figure 1)[33] might be required to reach high-quality white. As a matter of fact, the optimization of a tricomponent host:guest blend following a trial-error approach requires a huge effort with respect to time, costs, and wastes. Thus, a similar design of experiments analysis (D-optimal) was used to get the maximum information from the minimum number of experiments—see Experimental Section. The list of the entries is summarized in Table S6, Supporting Information. The active layer composition has been optimized in order to achieve the most efficient device keeping white emission. The

composition that allows to meet the two criteria ($\Delta E < 0.05$ and efficiency > 0.1 cd A^{-1}) corresponds to **1:2:3** in molar ratio of 0.977:10^{-6}:0.023—Figure S15, Supporting Information. Since the presence of **2** is marginal, **1:3** (0.977:0.023) devices were fabricated and they were driven at pulsed 10 mA cm^{-2}. According to the photoluminescence and frontier energy levels of **1** and **3**—Figure S16, Supporting Information, an efficient host:guest mechanism, in which **1** acts as a host featuring emission via electroluminescence and **3** is the guest being excited by either an efficient energy transfer process from the host to the guest or by a direct electron–hole recombination, was followed. These devices showed typical electrical LEC behavior—**Figure 5**, reaching a maximum value of efficiency 0.6 cd A^{-1} (EQE 0.3%) at ≈30 cd m^{-2} with stabilities of 2 h and 45 mJ. Much more relevant, device chromaticity corresponds to a white emission with x/y CIE color coordinates of 0.30/0.35, color correlated temperature of ≈6995 K, and CRI of 90. The chromaticity holds over the lifetime of the device (≈3 h), shifting toward the red in the final stage of the lifespan due to the different stabilities of **1** and **3**—Figure 5. Finally, it is interesting to point out that the performance for the first fully Cu-based white LEC represents a huge step forward with respect to the state-of-the-art white Cu-iTMC-LECs (0.05 cd A^{-1}@12 cd m^{-2}).[34]

3. Conclusion

This contribution shows a fresh approach using a multivariate analysis method to get meaningful statistic correlation

between X-ray structural and electronic features of [Cu(N^N)(P^P)]⁺ (>90 contributions database fine-tuned with theoretical calculations) and their photo-/electroluminescence responses applied to thin films (maximum PLQY at certain λ_{max} and maximum device efficiency at certain luminance) to predict the rational design of the best ligands for the first blue [Cu(N^N)(P^P)]⁺-based LEC that has been elusive over the last decades. A significant match between the predicted/experimental values was obtained after a full-fledge analysis of the X-ray structure, spectroscopic/microscopy/electrochemical of thin films, and the device optimization of the target blue-emitting complex **1** (λ_{max} = 488 nm/470 nm; PLQY of 47%/42%; 3.8 cd A⁻¹@170 cd m⁻²/3.6 cd A⁻¹@180 cd m⁻²) and the yellow-emitting complex **2** (λ_{max} = 590 nm/575 nm; PLQY of 25%/20%; 0.55 cd A⁻¹@30 cd m⁻²/0.60 cd A⁻¹@30 cd m⁻²) as a cross-check reference. While **1**-LECs represent the first functional blue LEC with [Cu(N^N)(P^P)]⁺, its performance is superior to blue LECs with tricoordinate Cu(I) complexes (0.17 cd A⁻¹@20 cd m⁻²) and Ir-iTMCs (average <2.2 cd A⁻¹@115 cd m⁻²). Still the device efficiency could be further maximized following well-known strategies to 1) control electrochemical doping stabilizing the position of the emitting neutral zone, 2) reduce microcavity effects, 3) increase light-outcoupling with microstructured electrodes and substrates, among others.[4] We further capitalized this approach to determine the best active layer composition to simultaneously maximize efficiency, luminance, and white color quality of the first all-[Cu(N^N)(P^P)]⁺-LECs host:guest LEC, realizing white light with CRI>90 and 0.6 cd A⁻¹@30 cd m⁻². This device outperforms previous [Cu(N^N)(P^P)]⁺:SM-based white-LECs (<0.05 cd A⁻¹@<12 cd m⁻²) as well as similar white LECs with CPs, QDs, SMs, and Ir-iTMCs (i.e., with CRI>90; average <0.3 cd A⁻¹@<70 cd m⁻²).

In view of these finding, this work teaches us a new way to rationalize the design of emitters and active layers in thin-film lighting. We strongly believe that a deeper understanding of the multivariate analysis model as first step toward advanced machine learning methods will be paramount for the fine design (mixing calculations/literature data in the model) of other emitters and charge transport materials that are prone to structural and electronic changes going from crystal powder, to solution, and to thin films. This is a current research focus in our labs to answer elusive challenges in the lighting field. As a first example, this paper has circumvented the fabrication of blue and white [Cu(N^N)(P^P)]⁺-based LECs achieving first-class performances.

4. Experimental Section

Multivariate Tools: The software MODDE (version 11.0.2.2309, Umetrics) was used. The authors defined 15 factors in total, namely: % buried volume of P∧P ligand (%V_bur PP) and % buried volume of ligands (%V_bur PP+NN),[46] distances between Cu–N1, Cu–N2 (with Cu–N1 > Cu–N2), Cu–P1, Cu–P2 (with Cu–P1 < Cu–P2), Cu···O, torsion angle of the N∧N ligand, total polar surface area of the ligand N∧N (tPSA NN), predicted partition coefficient (cLogP), bite angles of P∧P and N∧N ligands, HOMO and LUMO levels, and type of optoelectronic device (OLED or LEC). The responses collected were four: photoluminescence in thin film (λ_{max} and PLQY) and device performances (maximum luminance and efficiency). Based on literature, >90 entries were found.

The model was fitted with PLS method considering both first and second order terms. First-order terms considered the single factors independently, while second-order ones referred to interaction between factors. The coefficients of the multivariate regression equation are listed in Table S7, Supporting Information. With regard of active layer composition optimization toward white-LECs, the authors defined four relevant factors: 1) driving current density (10–200 mA cm⁻²), 2) blue (0.85–0.995), 3) orange (0–0.05), and 4) red molar ratio (0.005–0.1). The selected responses taken into account were both LEC performances (luminance, efficiency, and total emitted energy) and color quality (x/y CIE coordinates and ΔE). The response ΔE was defined as the trigonometric distance between the experimental x/y CIE coordinates and the equal energy point (0.33/0.33). The D-Optimal design showing the largest determinant of the X'X matrix was selected.

Synthesis and Characterization: When required, manipulations were performed using standard Schlenk techniques under dry nitrogen or an M. Braun glove box. Nitrogen was purified by passing through columns of supported P_2O_5 with moisture indicator, and of activated 4 Å molecular sieves. Anhydrous solvents were freshly distilled from appropriate drying agents. All chemicals were purchased from chemical suppliers and used without further purification. Liquid-chromatography coupled with high-resolution mass spectrometry (HPLC-HRMS) was performed in positive mode using a Thermo Fisher Ultimate3000 with Scientific Vanquish Flex UHPLC and a Thermo Fisher Orbitrap (Exactive Plus with Extend Mass Range: Source HESI II). The detector was a Vanquish PDA Detector (VF-XX, detection ≤ 5 ppm). Direct injection high-resolution mass spectrometry was used using as eluant HPLC grade acetonitrile. ¹H, ¹³C{¹H}, and ³¹P spectra were recorded using a Bruker Avance DPX-300 spectrometer. $CDCl_3$ and CD_2Cl_2 were dried over CaH_2, degassed by three freeze–pump–thaw cycles and stored on 4 Å molecular sieves prior to use. ¹H NMR spectra (300.13 MHz) were referenced to the residual protons of the deuterated solvent used. ¹³C{¹H} NMR spectra (75.47 MHz) were referenced internally to the D-coupled ¹³C resonances of the NMR solvent. ³¹P{¹H} NMR spectra (121 MHz) was referenced to external H_3PO_4. The ligands were synthesized following a modification of published procedures.[36,37]

*Synthesis of [Cu(Xanthphos)(N∧Nᵖʸ)](PF₆) (**1**)*: Under nitrogen atmosphere, [Cu(NCCH₃)₄](PF₆) (50 mg, 0.13 mmol) and Xanthphos (78 mg, 0.13 mmol) were mixed in 10 mL of dry CH_2Cl_2 and stirred at room temperature for 20 min. After this time, N∧Nᵖʸ (41 mg, 0.13 mmol) was added and stirred for additional 10 min. The mixture was filtered through celite and the filtrate concentrated to ≈2 mL by rotatory evaporation. The addition of diethyl ether caused the precipitation of a white solid, that was filtered, washed with diethyl ether, and dried under vacuum to give **1** (105 mg, 77%). Anal. Calcd. For $C_{59}H_{55}N_3CuF_6OP_3$ (1092.55): C, 64.68; H, 5.07; N, 3.85. Found: C, 64.71; H, 5.12; N, 3.43. TOF-MS (ES+): m/z [M⁺] = 946.3, 641.1 [Cu(Xanthphos)]⁺. ¹H NMR (300 MHz, CD2CL2, RT, δ): 7.63 (t, J = 8.0 Hz, 1H, H10 N∧Nᵖʸ), 7.59 (dd, J = 7.8 Hz, J2 = 1.4 Hz, 2H, H4 or H5 N∧Nᵖʸ), 7.55 (d, J = 8.3 Hz, 2H, H4 or H5 N∧Nᵖʸ), 7.47 (t, J = 7.4 Hz, 2H, H3 Xanthphos), 7.41 (d, J = 7.7 Hz, 1H, H9 or H11 N∧Nᵖʸ), 7.29 (t, J = 7.5 Hz, 4H, H12 Xanthphos), 7.21 (t, J = 7.5 Hz, 2H, H2 or H4 Xanthphos), 7.13 (t, J = 7.7 Hz, 2H H2 or H4 Xanthphos), 6.98 (dd, J = 14.3 Hz, J2 = 7.7 Hz, 8H, H11 Xanthphos), 6.74 (d, J = 8.2 Hz, 1H, H9 or H11 N∧Nᵖʸ), 6.63 (dd, J = 7.5 Hz, J2 = 5.0 Hz, J3 = 3.7 Hz, 8H, H10 Xanthphos), 2.54 (s, 3H, H18 or H19 N∧Nᵖʸ), 1.87 (s, 3H, H18 or H19 N∧Nᵖʸ), 1.55 (s, 6H, H8 Xanthphos), 1.12 (s, 9H, H8 N∧Nᵖʸ)—Figure S16, Supporting Information. ³¹P NMR (121.5 MHz, CD₂Cl₂, RT): −14.8 (s, 2P, Xanthphos), −144.0 (sept, PF₆).

*Synthesis of [Cu(Xanthphos)(N∧Nᵖᶻ)](PF₆) (**2**)*: This complex was prepared following the same methodology than for **1** but using [Cu(NCCH₃)₄](PF₆) (50 mg, 0.13 mmol), Xanthphos (78 mg, 0.13 mmol) and N∧Nᵖᶻ (41 mg, 0.13 mmol). Complex **2** was isolated as a yellow solid (120 mg, 77%). Anal. Calcd. For $C_{58}H_{54}N_4CuF_6OP_3$ (1093.53): C, 63.90; H, 4.98; N, 5.12. Found: C, 63.71; H, 4.57; N, 5.43. TOF-MS (ES+): m/z [M+] = 947.3, 641.1 [Cu(Xatnphos)]⁺. ¹H NMR (300 MHz, CD₂Cl₂, RT, δ):8.63 (s, 1H, H9 or H11 N∧Nᵖᶻ), 8.17 (s, 1H, H9 or H11 N∧Nᵖᶻ), 7.66–7.19 (m, aromatic, 14H), 7.16 (t, J = 7.7 Hz, 4H, H12 Xanthphos), 7.09–6.50 (m, aromatic, 12H), 6.24 (s, 1H, H16 N∧Nᵖᶻ), 2.61 (s, 3H,

H18, or H19 N∧N^{pz}), 1.87 (s, 3H, H18, or H19 N∧N^{pz}), 1.58 (s, 6H, H8 Xanthphos), 1.20 (s, 9H, H8 N∧N^{pz})—Figure S17, Supporting Information. ^{31}P NMR (121.5 MHz, CD$_2$Cl$_2$, RT): −13.9 (s, 2P, Xanthphos), −144.0 (sept, PF$_6$).

X-ray Crystallography: Crystals of each sample were mounted on MiTeGen MicroLoop sample holders and fixed in the cold nitrogen stream on a diffractometer. Diffraction intensities were recorded al low temperature on a Bruker D8 Venture diffractometer, equipped with a TXS rotating anode source (Mo-Kα radiation), a Helios optic, and a Photon 100 CMOS detector (1) or a Bruker D8 Venture diffractometer, equipped with a IµS microfocus source (Mo-Kα radiation), a Helios optic and a Photon II CPAD detector (2) using the APEX3 software package.[47] A matrix scan was used to determine the initial lattice parameters. Reflections were corrected for Lorentz and polarization effects, scan speed, and background using SAINT.[48] Absorption correction, including odd and even ordered spherical harmonics was performed using SADABS.[49] Space group assignment was based upon systematic absences, E statistics, and successful refinement of the structures. The structures were solved using SHELXT with the aid of successive difference Fourier maps, and were refined against all data using SHELXL in conjunction with SHELXLE.[50–52] The hydrogen atoms were calculated in ideal positions as follows: methyl hydrogen atoms were refined as part of rigid rotating groups with a C–H distance of 0.98 Å and $U_{iso(H)} = 1.5U_{eq(C)}$. Other H atoms were placed in calculated positions and refined using a riding model, with methylene and aromatic C–H distances of 0.99 and 0.95 Å, respectively, and other C–H distances of 1.00 Å, all with $U_{iso(H)} = 1.2U_{eq(C)}$. Non-hydrogen atoms were refined with anisotropic displacement parameters. Full-matrix least-squares refinements were carried out by minimizing $\Sigma w(F_o^2 - F_c^2)^2$ with the SHELXL weighting scheme.[4] Neutral atom scattering factors for all atoms and anomalous dispersion corrections for the non-hydrogen atoms were taken from International Tables for Crystallography.[53] Images of the crystal structures were generated with Mercury.[54]

Theoretical Characterization: All the calculations were performed by the Gaussian 16 program package,[55] employing DFT and time dependent (TD)-DFT methods,[56,57] the Becke three-parameter hybrid functional,[58] and the Lee–Yang–Parr gradient-corrected correlation functional (B3LYP).[59] The solvent effect was included by using the conductor-like polarizable continuum model with DCM as solvent.[60,61] The LanL2DZ basis set[62] and effective core potential were used for the Cu atom and the 6-31G** basis set[63] was used for all the other atoms. Geometry optimizations of the ground state and the lowest-lying triplet state (T$_1$) were carried out without any symmetry constraints. The nature of the optimized structures was verified by using harmonic vibrational frequency calculations. No imaginary frequencies were found. The UV–vis electronic absorption spectrum in the ground state was simulated computing a total of 128 singlet excited states by using TD-DFT. The electronic distribution and the localization of the singlet excited states were visualized by using electron-density difference maps (EDDMs). GaussSum 2.2.5[64] was used to simulate the theoretical UV–vis spectrum and for extraction of EDDMs.[65] Molecular-graphic images were produced by using the UCSF Chimera package from the Re source for Biocomputing, Visualization, and Informatics at the University of California, San Francisco (supported by NIH P41 RR001081).[66]

Spectroscopic, Electrochemical, and Microscopy Characterization: Absorption spectra were recorded with a Shimadzu UV–vis/2600 spectrometer. The photoluminescence spectra and PLQY values at 25 °C were measured with an FS5 Spectrofluorometer with an integrating sphere for absolute PLQY valuation (Edinburgh Instruments). Photoluminescence measurements at temperatures ranging from 77 to 400 K were performed upon enclosing **1-** and **2-** based thin films in a Optistat-DN (Oxford Instruments) equipped with a temperature controller. Excited state decay lifetimes (τ) were obtained with a microsecond flashlamp (λ_{exc} = 330 nm, 100 Hz and λ_{exc} = 400 nm, 100 Hz for **1** and **2**, respectively). The photoluminescence spectra were acquired 10 min after the sample reached the desired temperature in order to ensure complete sample thermalization. The average lifetime could be obtained with the following formula:

$$\tau = \frac{A_1\tau_1^2 + A_2\tau_2^2}{A_1\tau_1 + A_2\tau_2} \tag{3}$$

Cyclic voltammetry was performed in acetonitrile solution, using the redox couple Cp$_2$Fe/Cp$_2$Fe$^+$ as reference. Solution of tetrabutylammonium hexafluorophosphate 0.1 M was used as electrolyte, and Pt disk/Pt wire/Ag/Ag$^+$ electrodes as working/counter/reference electrodes. It was measured with a Metrohm µAutolabIII potentiostat, at 100 mV s^{-1}.

Thin films were prepared from a filtered solution of **1** and **2** (10 mg mL^{-1} in *n*-butanone; without or with IL, as below described) using a spin-coated technique at 1500 rpm for 30 s.

Topography images were acquired with a MFP-3D Origin+ AFM (Asylum Research) and they were elaborated with Gwyddion evaluation software.

Device Fabrication and Measurement: Indium–tin oxide (ITO) substrates were purchased from Naranjo Substrates with an ITO thickness of 130 nm. They were extensively clean using detergent, water, ethanol, and propan-2-ol as solvents in an ultrasonic bath (frequency 37–70 Hz) for 15 min each. Afterward, the slides were dried, and they were positioned in UV–ozone cleaner for 8 min. The clean plates were coated with 70 nm PEDOT:PSS layers via spin-coating. To this end, an aqueous solution of PEDOT:PSS was filtered and mixed with propan-2-ol in a ratio of 3:1. From this solution, 50 µL was dropped onto the substrate at a rotation speed of 2000 rpm and spun for 60 s. The resulting layers were dried on a hotplate at 120 °C. Stock solutions of **1**, **2**, **3**, and BMIMPF$_6$ were prepared in *n*-butanone at concentration of 10 mg mL^{-1} for the complexes and 15 mg mL^{-1} for the latter. Active layers (≈120 nm) were deposited from a sample solution, achieved combining the corresponding stock solutions in the desired ratio, spin-coated at 1500 rpm for 30 s. In all cases, after the deposition of the active layer, the devices were dried under vacuum for 2 h and transferred to an inert atmosphere glovebox (<0.1 ppm O$_2$ and H$_2$O, Angstrom Engineering). Finally, aluminum cathodes (90 nm) were thermally evaporated onto the active layer using a shadow mask under high vacuum (<1 × 10^{-6} mbar) in an Angstrom Covap evaporator integrated into the inert atmosphere glovebox. The device statistics involved up to five different devices, that is, a total number of 20 pixels.

Time dependence of luminance, voltage, and current was measured by applying pulsed voltage and monitoring the desired parameters simultaneously using an Avantes spectrophotometer (Avaspec-ULS2048L-USB2) in conjunction with a calibrated integrated sphere Avasphere 30-Irrad and Botest OLT OLED Lifetime-Test System. The temperature of the devices upon driving was recorded with a FLIR 430-sc thermal camera. EIS assays were carried out with a potentiostat/galvanostat (Metrohm µAutolabIII) equipped with a frequency response analyzer module (FRA2). Measurements were performed at the applied voltage range from 0 to 5 V and fitted with the Nova software using the circuit model shown in Figure S12, Supporting Information. The AC signal amplitude was set to 10 mV and modulated in a frequency range from 10 to 10^6 Hz. The CPE element was typically used to consider 1) the surface roughness of the electrodes and active layers, 2) inhomogeneous growing of the doped fronts using different active layer compositions and driving conditions, and 3) nonuniform electric field and/or current distribution across the active layer due to the morphology and thickness of the active layers. Ionic conductivity and dielectric constant were extrapolated from the fitted data following the procedure reported elsewhere.[67]

Supporting Information

Supporting Information is available from the Wiley Online Library or from the author.

**ADVANCED
SCIENCE NEWS**

www.advancedsciencenews.com

**ADVANCED
MATERIALS**

www.advmat.de

Acknowledgements

Conflict of Interest

The authors declare no conflict of interest.

Data Availability Statement

The data that support the findings of this study are available from the corresponding author upon reasonable request.

Keywords

[1] Q. Pei, R. D. Costa, *Adv. Funct. Mater.* **2020**, *30*, 2002879.

[2] R. D. Costa, *Light-Emitting Electrochemical Cells*, Springer International Publishing, Cham, Switzerland **2017**.

[3] S. Tang, A. Sandström, P. Lundberg, T. Lanz, C. Larsen, S. van Reenen, M. Kemerink, L. Edman, *Nat. Commun.* **2017**, *8*, 1190.

[4] K. Youssef, Y. Li, S. O'Keeffe, L. Li, Q. Pei, *Adv. Funct. Mater.* **2020**, *30*, 1909102.

[5] a) R. Bai, X. Meng, X. Wang, L. He, *Adv. Funct. Mater.* **2020**, *30*, 1907169; b) The average stabilities are calculated for all the contributions described in 5a without discriminating device architecture and driving conditions.

[6] S. Kanagaraj, A. Puthanveedu, Y. Choe, *Adv. Funct. Mater.* **2020**, *30*, 1907126.

[7] E. Nannen, J. Frohleiks, S. Gellner, *Adv. Funct. Mater.* **2020**, *30*, 1907349.

[8] S. Tang, L. Edman, *Top. Curr. Chem.* **2016**, *374*, 40.

[9] E. Fresta, R. D. Costa, *J. Mater. Chem. C* **2017**, *5*, 5643.

[10] M. H. Bowler, A. Mishra, A. C. Adams, C. L. D. Blangy, J. D. Slinker, *Adv. Funct. Mater.* **2020**, *30*, 1906715.

[11] K. Matsuki, J. Pu, T. Takenobu, *Adv. Funct. Mater.* **2020**, *30*, 1908641.

[12] K. Schlingman, Y. Chen, R. S. Carmichael, T. B. Carmichael, *Adv. Mater.* **2021**, *33*, 2006863.

[13] a) C. Zhang, R. Liu, D. Zhang, L. Duan, *Adv. Funct. Mater.* **2020**, *30*, 1907156; b) The average stabilities are calculated for all the contributions described in 13a without discriminating device architecture and driving conditions.

[14] H. Su, Y. Chen, K. Wong, *Adv. Funct. Mater.* **2020**, *30*, 1906898.

[15] G. U. Mahoro, J. Fernandez-Cestau, J. Renaud, P. B. Coto, R. D. Costa, S. Gaillard, *Adv. Opt. Mater.* **2020**, *8*, 2000260.

[16] C. E. Housecroft, E. C. Constable, *J. Mater. Chem. C*, https://doi.org/10.1039/d1tc04028f.

[17] M. D. Weber, E. Fresta, M. Elie, M. E. Miehlich, J.-L. Renaud, K. Meyer, S. Gaillard, R. D. Costa, *Adv. Funct. Mater.* **2018**, *28*, 1707423.

[18] M. Elie, F. Sguerra, F. Di Meo, M. D. Weber, R. Marion, A. Grimault, J.-F. Lohier, A. Stallivieri, A. Brosseau, R. B. Pansu, J.-L. Renaud, M. Linares, M. Hamel, R. D. Costa, S. Gaillard, *ACS Appl. Mater. Interfaces* **2016**, *8*, 14678.

[19] X.-L. Chen, C.-S. Lin, X.-Y. Wu, R. Yu, T. Teng, Q.-K. Zhang, Q. Zhang, W.-B. Yang, C.-Z. Lu, *J. Mater. Chem. C* **2015**, *3*, 1187.

[20] L. P. Ravaro, K. P. S. Zanoni, A. S. S. de Camargo, *Energy Rep.* **2020**, *6*, 37.

[21] X.-L. Chen, R. Yu, Q.-K. Zhang, L.-J. Zhou, X.-Y. Wu, Q. Zhang, C.-Z. Lu, *Chem. Mater.* **2013**, *25*, 3910.

[22] M. J. Leitl, D. M. Zink, A. Schinabeck, T. Baumann, D. Volz, H. Yersin, *Top. Curr. Chem.* **2016**, *374*, 25.

[23] E. Fresta, G. Volpi, C. Garino, C. Barolo, R. D. Costa, *Polyhedron* **2018**, *140*, 129.

[24] M. D. Weber, C. Garino, G. Volpi, E. Casamassa, M. Milanesio, C. Barolo, R. D. Costa, *Dalton Trans.* **2016**, *45*, 8984.

[25] C. Li, C. F. R. R. MacKenzie, S. A. Said, A. K. Pal, M. A. Haghighatbin, A. Babaei, M. Sessolo, D. B. Cordes, A. M. Z. Z. Slawin, P. C. J. J. Kamer, H. J. Bolink, C. F. Hogan, E. Zysman-Colman, *Inorg. Chem.* **2021**, *60*, 10323.

[26] A. Schinabeck, J. Chen, L. Kang, T. Teng, H. H. H. Homeier, A. F. Suleymanova, M. Z. Shafikov, R. Yu, C.-Z. Lu, H. Yersin, *Chem. Mater.* **2019**, *31*, 4392.

[27] R. Czerwieniec, M. J. Leitl, H. H. H. Homeier, H. Yersin, *Coord. Chem. Rev.* **2016**, *325*, 2.

[28] H. Yersin, R. Czerwieniec, M. Z. Shafikov, A. F. Suleymanova, *ChemPhysChem* **2017**, *18*, 3508.

[29] R. Czerwieniec, J. Yu, H. Yersin, *Inorg. Chem.* **2011**, *50*, 8293.

[30] J. L. Baker, L. H. Jimison, S. Mannsfeld, S. Volkman, S. Yin, V. Subramanian, A. Salleo, A. P. Alivisatos, M. F. Toney, *Langmuir* **2010**, *26*, 9146.

[31] S. C. B. Mannsfeld, M. L. Tang, Z. Bao, *Adv. Mater.* **2011**, *23*, 127.

[32] D. R. Blasini, J. Rivnay, D.-M. Smilgies, J. D. Slinker, S. Flores-Torres, H. D. Abruña, G. G. Malliaras, *J. Mater. Chem.* **2007**, *17*, 1458.

[33] E. Fresta, M. D. Weber, J. Fernandez-Cestau, R. D. Costa, *Adv. Opt. Mater.* **2019**, *7*, 1900830.

[34] E. Fresta, G. U. Mahoro, L. M. Cavinato, J.-F. Lohier, J.-L. Renaud, S. Gaillard, R. D. Costa, *Adv. Opt. Mater.*, https://doi.org/10.1002/adom.202101999.

[35] E. Fresta, R. D. Costa, *Adv. Funct. Mater.* **2020**, *30*, 1908176.

[36] J. Fernandez-Cestau, B. Bertrand, M. Blaya, G. A. Jones, T. J. Penfold, M. Bochmann, *Chem. Commun.* **2015**, *51*, 16629.

[37] C. D. Sunesh, M. S. Subeesh, K. Shanmugasundaram, R. K. Chitumalla, J. Jang, Y. Choe, *Dyes Pigm.* **2016**, *128*, 190.

[38] E. Fresta, G. Volpi, M. Milanesio, C. Garino, C. Barolo, R. D. Costa, *Inorg. Chem.* **2018**, *57*, 10469.

[39] L. Yang, D. R. Powell, R. P. Houser, *Dalton Trans.* **2007**, 955.

[40] M. D. Weber, J. E. Wittmann, A. Burger, O. B. Malcıoğlu, J. Segarra-Martí, A. Hirsch, P. B. Coto, M. Bockstedte, R. D. Costa, *Adv. Funct. Mater.* **2016**, *26*, 6737.

[41] Y. Gao, R. C. I. MacKenzie, Y. Liu, B. Xu, P. H. M. van Loosdrecht, W. Tian, *Adv. Mater. Interfaces* **2015**, *2*, 1400555.

[42] E. Fresta, J. Dosso, J. Cabanillas-Gonzalez, D. Bonifazi, R. D. Costa, *ACS Appl. Mater. Interfaces* **2020**, *12*, 28426.

[43] Z.-P. Yang, H.-C. Su, *Adv. Funct. Mater.* **2020**, *30*, 1906788.

[44] E. Fresta, K. Baumgärtner, J. Cabanillas-Gonzalez, M. Mastalerz, R. D. Costa, *Nanoscale Horiz.* **2020**, *5*, 473.

[45] L. D. Bastatas, M. D. Moore, J. D. Slinker, *ChemPlusChem* **2018**, *83*, 266.

[46] M. Alkan-Zambada, E. C. Constable, C. E. Housecroft, *Molecules* **2020**, *25*, 2647.

[47] U. Inc., Bruker AXS, Madison, Wisconsin, "APEX suite of crystallographic software, APEX 3, Version 2015.5 2," **2015**.

[48] U. Inc., Bruker AXS, Madison, Wisconsin, "SAINT, Version 8.38A," **2017**.

[49] U. Inc., Bruker AXS, Madison, Wisconsin, "SADABS, Version 2016/2," **2016**.

[50] G. M. Sheldrick, *Acta Crystallogr., Sect. C: Struct. Chem.* **2015**, *71*, 3.

[51] G. M. Sheldrick, *Acta Crystallogr., Sect. A: Found. Adv.* **2015**, *71*, 3.

[52] C. B. Hübschle, G. M. Sheldrick, B. Dittrich, *J. Appl. Crystallogr.* **2011**, *44*, 1281.

[53] A. J. C. Wilson, V. Geist, *Cryst. Res. Technol.* **1993**, *28*, 110.

[54] C. F. Macrae, I. J. Bruno, J. A. Chisholm, P. R. Edgington, P. McCabe, E. Pidcock, L. Rodriguez-Monge, R. Taylor, J. van de Streek, P. A. Wood, *J. Appl. Crystallogr.* **2008**, *41*, 466.

[55] M. J. Frisch, G. W. Trucks, H. B. Schlegel, G. E. Scuseria, M. A. Robb, J. R. Cheeseman, G. Scalmani, V. Barone, G. A. Petersson, H. Nakatsuji, X. Li, M. Caricato, A. V. Marenich, J. Bloino, B. G. Janesko, R. Gomperts, B. Mennucci, H. P. Hratchian, J. V. Ortiz, A. F. Izmaylov, J. L. Sonnenberg, D. Williams-Young, F. Ding, F. Lipparini, F. Egidi, J. Goings, B. Peng, A. Petrone, T. Henderson, D. Ranasinghe, et al. Gaussian 16, Revision C.01, Gaussian, Inc., Wallingford, CT, USA 2016.

[56] A. C. Hurley, *Introduction to the Electron Theory of Small Molecules*, Academic Press, London, UK **1976**.

[57] R. E. Stratmann, G. E. Scuseria, M. J. Frisch, *J. Chem. Phys.* **1998**, *109*, 8218.

[58] A. D. Becke, *J. Chem. Phys.* **1993**, *98*, 5648.

[59] C. Lee, W. Yang, R. G. Parr, *Phys. Rev. B* **1988**, *37*, 785.

[60] M. Cossi, G. Scalmani, N. Rega, V. Barone, *J. Chem. Phys.* **2002**, *117*, 43.

[61] J. Tomasi, B. Mennucci, R. Cammi, *Chem. Rev.* **2005**, *105*, 2999.

[62] W. J. Hehre, *Acc. Chem. Res.* **1976**, *9*, 399.

[63] M. J. Frisch, J. A. Pople, J. S. Binkley, *J. Chem. Phys.* **1984**, *80*, 3265.

[64] N. M. O'boyle, A. L. Tenderholt, K. M. Langner, *J. Comput. Chem.* **2008**, *29*, 839.

[65] M. Head-Gordon, A. M. Grana, D. Maurice, C. A. White, *J. Phys. Chem.* **1995**, *99*, 14261.

[66] E. F. Pettersen, T. D. Goddard, C. C. Huang, G. S. Couch, D. M. Greenblatt, E. C. Meng, T. E. Ferrin, *J. Comput. Chem.* **2004**, *25*, 1605.

[67] E. Fresta, J. Dosso, J. Cabanillas-González, D. Bonifazi, R. D. Costa, *Adv. Funct. Mater.* **2020**, *30*, 1906830.